How SARS CoV-2 Omicron Droplets Transport and Deposit in Realistic Extrathoracic Airways

Mohammad S. Islam[1*], Md. Mizanur Rahman[2,3], Akbar Arsalanloo[4], Hamidreza Mortazavy Beni[5], Puchanee Larpruenrudee[1], Nick S. Bennett[1], Richard Collins[6], Tevfik Gemci[7], Maureen Taylor[8] and YuanTong G[9]

[1] School of Mechanical and Mechatronic Engineering, University of Technology Sydney (UTS), 15 Broadway, Ultimo, NSW-2007, Australia
[2] School of Engineering, Design and Built Environment, Western Sydney University, Penrith, NSW 2751, Australia.
[3] Department of Mathematics, Faculty of Science, Islamic University, Kushtia-7003, Bangladesh.
[4] Department of Mechanical Engineering, Faculty of Engineering, Urmia University, Urmia-30200, Iran
[5] Department of Biomedical Engineering, Arsanjan Branch, Islamic Azad University, Arsanjan, Iran.
[6] Biomechanics International, Cranberry Township, PA 16066, USA.
[7] Synergy CFD Consulting, Las Vegas, NV 89146, USA.
[8] School of Communication, University of Technology Sydney (UTS), 15 Broadway, Ultimo, NSW-2007, Australia
[9] School of Mechanical, Medical and Process Engineering, Faculty of Engineering, Queensland University of Technology, Brisbane, QLD 4000, Australia.

Corresponding author: mohammadsaidul.islam@uts.edu.au

Abstract

The SARS CoV-2 Omicron variant is more highly transmissible and causes a higher mortality rate compared to the other eleven variants despite the high vaccination rate. The Omicron variant also establishes a local infection at the extrathoracic airway level. For better health risk assessment of the infected patients, it is essential to understand the transport behaviour and the toxicity of the Omicron variant droplet deposition in the extrathoracic airways, which is missing in the literature. Therefore, this study aims to develop a numerical model for the Omicron droplet transport to the extrathoracic airways and to analyze that transport behaviour. The Finite Volume method and ANSYS Fluent 2020 R2 solver were used for the numerical simulation. The Lagrangian approach, Discrete Phase model and Species Transport model were employed to simulate the Omicron droplet transport and deposition. Different breathing rates, the mouth and nose inhalation methods were employed to analyzed the viral toxicity at the airway wall. The results from this study indicated that there was a 33% of pressure drop for a flowrate at 30 L/min, while there was only a 3.5% of pressure drop for a 7.5 L/min. The nose inhalation of SARS CoV-2 Omicron droplets is significantly more harmful than through the mouth due to a high deposition rate at the extrathoracic airways and high toxicity in the nasal cavities. The

findings of this study would potentially improve knowledge of the health risk assessment of Omicron-infected patients.

Keywords: SARS CoV-2 Omicrons, Droplets, Toxicity, Extrathoracic airways, Drug delivery.

Nomenclature

A_p	Aerosol area, m^2
C_C	Cunningham factor
C_D	Drag coefficient
d_p	Aerosol diameter, m
e	Specific internal energy
F_D	Drag force, N
g_i	Force gravity, m s^{-2}
G_{k_t}	Generation of turbulent kinetic energy due to mean velocity gradients
G_b	Generation of turbulent kinetic energy due to mean velocity gradients buoyancy
I	Turbulent intensity
k_B	Boltzmann constant
k_t	Turbulent kinetic energy
Q	Flow rate, L/min
Re	Reynolds number
S_{k_t}	Turbulent kinetic energy source term, J
S_{ε_t}	Turbulent dissipation source term, J
S_o	Spectral intensity
T	Temperature, K
t	time, s
U	Time-averaged velocity, m s^{-1}
u_i'	Fluctuating velocity, m s^{-1}
v_r	Velocity of particle, m s^{-1}
Y_M	Contribution of the fluctuating dilatation in compressible turbulence to the overall dissipation rate

Greek

ε_t	Turbulent dissipation rate
σ_{ε_t}	Turbulent Prandtl number for ε_t
σ_{k_t}	Turbulent Prandtl number for k_t
λ	Thermal conductivity, W m^{-1} K^{-1} or gas molecules' mean free path
μ	Dynamic viscosity, Pa s
v	Kinematic viscosity, m^2 s^{-1}
ρ	Density, kg m^{-3}

Subscript

g	Air
f	Airflow
p	Aerosol particle

Abbreviation

DE	deposition efficiency

Introduction

During the breathing process, the air entering the respiratory system often contains foreign aerosols, which in some cases may be accompanied by viral contamination that is harmful to the body [1]. Inhalation of viral particles is of significant health concern since these conditions are more critical for crowded indoor environmental quality (IEQ) [2]. The natural physiological function of the nose makes it possible to purify the incoming air by trapping suspended particles in the nasal hair or cilia. Despite this filtration, not all the particles entering the nasal cavity are deposited as some of those particles can enter the lungs, which may lead to severe damage [3].

In terms of the SARS CoV-2 virus, one of the methods of transmission of the SARS CoV-2 virus is through infected droplets [4]. Viral droplets enter the host body through nose and mouth inhalation.

Research shows that significant amounts of infected droplets are produced when an infected person with COVID-19 talks, coughs, and sneezes [5]. Various indexes such as exposure time and the intensity of the airflow rate coming out of the respiratory system of an infected person are important [6, 7]. Also, approximately 59%-82% of patients experience coughing during their illness [8], which exacerbates the problem. A cough is prone to eject significant amounts of viral droplets into the surroundings. Without wearing a mask, there are around 13,000 particles that are released during coughing per person [9]. There is around 11.2 m/s of the release speed for coughing conditions based on the experimental measurement by Gupta et al. [10]. Therefore, the more air is inhaled from the environment, including indoor environments, which then become contaminated with the COVID-19 virus, the more likely it is to transmit the viral disease to others. At the same time, around 40%-45% of people may be asymptomatic, so these people contaminate the air more often, even through talking or normal breathing [8]. Viral droplets of different sizes are expected to be present in any contaminated environment. Therefore, they enter the respiratory system during inspiration, creating disease conditions after viral droplet deposition. As we move more deeply into the respiratory system, the droplet size produced becomes smaller so that the droplet size produced in bronchioles and the oral cavity is equal to 1.8 μm and 374 μm, respectively [11]. The more detailed studies of air and particle flows in the airways would increase the knowledge of what causes the biological agent to deposit in the respiratory system [12, 13]. Preliminary studies on airborne particles and airflow within the respiratory system are generally based on theoretical and laboratory research, focusing on velocity and efficiency diagrams [1]. There are several methods that have been used to study the distribution of particles in the lungs, including medical imaging [4]. By all of these methods, the patient must inhale a Radioactive Tracer Gas, which can be very harmful. The computational fluid dynamics (CFD) method has been employed to study the airflow characteristics, particle transport and deposition within the human airways. This method provides more accurate information from the required data, which cannot easily be obtained through experimental experiments.

Since the study of droplet movement and deposition is complicated, researchers often assume the droplet is a spherical particle for simulation purposes. Heyder, et al.[14] studied particle deposition for four volunteers. In this experiment, spherical particles with a diameter of 0.2 μm to 1 μm, were considered, a respiration volume of 500 ml, and an uninterrupted respiration of 4 seconds. The basis for calculating the deposition efficiency was based on the density of particles sitting on the wall. They compared their results with previous experimental work and found that their lower deposition efficiency was due to uninterrupted breathing; this stop can lead to increased particle deposition in the respiratory system. Ferron, et al.[15] examined particle transport in the entire respiratory system. The study reports that the aerosols that enter

through the nose are higher than those that enter through the mouth to the trachea and bronchi. Cheng, et al.[16] obtained similar results in the study of particle deposition efficiency in a model made of oral-tracheal cavity and bronchus under different respiratory flow rates. They found that at a flow rate of 60 L/min, 90% of particles with a diameter of more than 20 μm deposit in the oral cavity. Zhou and Cheng[17] used the method of Cheng, et al.[16] and showed that the viral aerosol deposition in the presence of the larynx is greater than in the absence of the larynx. It is evident from the previous study that respiratory infection could happen due to the smaller diameter of virus droplet transport to the respiratory system [18]. The smaller droplet can be suspended in the atmospheric air longer and transmitted to the respiratory system during inhalation. Islam, et al.[2] analyzed the smaller SARS CoV-2 aerosol transport to the lower airways. However, the study does not consider the extrathoracic airways, and the inert aerosols are considered for the analysis. In reality, SARS CoV-2 Omicron virus transmits as droplets during coughing and sneezing, and they enter into the extrathoracic airways during inhalation. For precise knowledge of the SARS CoV-2 Omicron transport in extrathoracic airways, droplets should be considered instead of inert particles [19]. From the stated reports in the literature, studies used inert aerosol to represent the virus transport in the extrathoracic airways.

Therefore, this study aims to develop an advanced numerical model for the SARS CoV-2 Omicron droplet transport and deposition in the extrathoracic airways of a realistic model. The primary purpose of this study is to analyze the SARS CoV-2 Omicron droplet deposition pattern, toxicity at the airway wall and deposition hotspot under various physical activity conditions. The study also aims to analyze the mouth and nose inhalation of the SARS CoV-2 Omicron droplet, and their impacts on overall transport. The comprehensive analysis of this first-ever SARS CoV-2 Omicron droplet transport in the extrathoracic airways could improve the health risk assessment of the COVID patients.

Numerical Methods

The numerical simulations were performed for various physical activity conditions to investigate the SARS coronavirus-2 Omicron transport in extrathoracic airways. These include the flowrates at 7.5 L/min, 15 L/min, and 30 L/min. ANSYS-FLUENT 2020 R2, Lagrangian approach, Discrete Phase Model (DPM) and Specise Transport models were used to solve the fluid flow and SARS CoV-2 Omicron droplet transport. The mass equation and momentum equation were used to calculate the fluid flowfield as Equation (1) and Equation (2), respectively [20, 21].

$$\frac{\partial \rho}{\partial t} + \nabla \cdot (\rho \vec{v}) = 0, \tag{1}$$

$$\nabla \cdot (\rho \vec{v} \vec{v}) = -\nabla p + \nabla \cdot \left(\mu \left(\nabla \vec{v} + \nabla \vec{v}^{T} \right) \right) + \rho \vec{g}, \tag{2}$$

where p and μ are static pressure and molecular viscosity, respectively. The gravitational body force is defined as $\rho\vec{g}$.

The internal energy is calculated by the following equation [17];

$$\nabla \cdot (\rho \vec{v} e) = -\nabla \cdot \vec{j}, \tag{3}$$

where e is the specific internal energy, and $\vec{j}$ is the heat flux vector which is the sum of contributions due to heat condition and enthalpy diffusion effects.

Due to the high anatomical complexity in the mouth-throat areas, there is no established velocity profile during the inhalation. Studies to date used the uniform one-way inhalation [22] and parabolic [23] inlet conditions for the simulation. The uniform flow distribution becomes parabolic at the tracheal section where the flow becomes fully developed. This study employs uniform inlet conditions at the mouth-throat inlet based on three different flowrates to represent the daily physical activities for SARS coronavirus-2 Omicron transport in extrathoracic airways. These include the flowrates at 7.5 L/min, 15 L/min, and 30 L/min. The pressure outlet condition was used at the exit of the extrathoracic model. In the real case, there is a small pressure variation when the airflow is flowing from the upper generation to the lower generation of the human airways. This was not considered in the current study in which the whole model and open outlet conditions are used. The Reynolds number (Re) of the airflow can be calculated by $Re_f = \frac{v_f \cdot d_a}{\mu_f}$, where v_f and μ_f are the velocity and dynamic viscosity of the airflow and d_a is the airway diameter. The Re of the highest flow rate was taken as 2546.

The realisable k-ε turbulence model [24, 25] is considered a viscous model with scalable wall functions for near-wall treatment. The scalable wall function was selected as it demonstrates a superior ability to capture the mean flow of the complex structures [26, 27]. The kinetic energy equation is expressed as:

$$\frac{\partial}{\partial t}(\rho k) + \frac{\partial}{\partial x_j}(\rho k u_j) = \frac{\partial}{\partial x_j}\left[\left(\mu + \frac{\mu_t}{\sigma_k}\right)\frac{\partial k}{\partial x_j}\right] + G_k + G_b - \rho\varepsilon_t - Y_M + S_k \tag{4}$$

The dissipation rate of the turbulent kinetic energy equation is defined as:

$$\frac{\partial}{\partial t}(\rho \varepsilon) + \frac{\partial}{\partial x_j}(\rho \varepsilon u_j) = \frac{\partial}{\partial x_j}\left[\left(\mu + \frac{\mu_t}{\sigma_\varepsilon}\right)\frac{\partial \varepsilon}{\partial x_j}\right] + \rho C_1 S\varepsilon - \rho C_2 \frac{\varepsilon^2}{k+\sqrt{v\varepsilon}} + C_{1,\varepsilon}\frac{\varepsilon}{k}C_{3,\varepsilon}G_b + S_\varepsilon, \tag{5}$$

where the constant coefficients have values: $C_{1,\varepsilon} = 1.44$, $C_2 = 1.9$, $\sigma_k = 1.0$, and $\sigma_\varepsilon = 1.2$. G_k and G_b is the turbulence kinetic energy production induced by mean velocity gradients and buoyancy, respectively. The contribution of the fluctuating dilatation in the incompressible turbulence to the overall dissipation rate is expressed as Y_M. The turbulent viscosity is defined as $\mu_t = \rho C_\mu \frac{k^2}{\varepsilon}$ [28]. The

k-ε turbulence model is the most common model for the CFD method to simulate mean flow characteristics for turbulent flow conditions. This model is widely used to validate turbulence models with applications from industrial and environmental flows [26, 29, 30]. However, it should be noted that the limitation of this model is having a problem when dealing with unconfined flows [31], curved boundary layers, rotating flows and flow in non-circular ducts [32].

In general, the SARS coronavirus-2 viruses could aggregate or transport as droplets during some activities such as exhalation, coughing, or sneezing. These can increase the overall diameters of the virus-laden aerosol particles [33, 34]. Therefore, various droplet sizes (nano and micro sizes) are selected in this study including 500 nm, 800 nm, 1 μm, 2.5 μm, 5 μm, and 10 μm. It is important to include Brownian motion for the smaller diameter particle transport (Equation (6) to Equation (10)) [2, 35].

$$\frac{dv_i^p}{dt} = F_D + F_{Brownian} + F_{Lift} + \frac{\rho_p - \rho_g}{\rho_p} g_i,$$

$$F_D = \frac{1}{C_c} C_D A_p \frac{\rho_g |v_i^g - v_i^p| (v_i^g - v_i^p)}{2m_p} = \frac{18\mu_g}{\rho_p d_p^2 C_c} \left(v_i^g - v_i^p\right), \tag{6}$$

$$C_c = 1 + \frac{2\lambda}{d_p}\left(1.257 + 0.4e^{-\frac{1.1 d_p}{2\lambda}}\right),$$

where F_D and C_D are the forces due to drag and drag coefficient. A_p and λ are the aerosol areas and gas molecules' mean free path, respectively. The densities of the aerosol particles and the air are defined as ρ_p and ρ_g, respectively. g_i is the force of gravity, μ_g is the gas viscosity and d_p is the aerosol diameter. The C_C is the Cunningham factor which is dependent on the droplet size. Table 1 summarises the value of this factor relative to the droplet size.

Table 1. The Cunningham factor for smaller droplet size

Droplet Size	500 nm	800 nm	1000 nm
C_C	1.20	1.20	1.17

For a low Reynolds number of the particle flows (Re_p) which is less than 0.5, the drag coefficient (C_D) is defined as [36]

$$C_D = \frac{24}{Re_p}, \qquad Re_p < 0.5. \tag{7}$$

The particle Reynolds number is expressed as [37]

$$Re_p = \rho_g \frac{d_p |v_r|}{\mu_g} \tag{8}$$

where v_r denotes the relative velocity.

The amplitude for the Brownian force is calculated by [38]

$$F_{Brownian} = \zeta\sqrt{\frac{\pi S_o}{\Delta t}}, \tag{9}$$

where ζ is the unit variance for an independent Gaussian random number; time-step integration of the particle is defined as Δt. S_o is the spectral intensity that is determined by [38, 39]

$$S_o = \frac{216\mu k_B T}{\pi^2 \rho_p d_p^5 \left(\frac{\rho_p}{\rho_g}\right)^2 C_c}, \tag{10}$$

where T refers to absolute fluid temperature, k_B is the Boltzmann constant, and ρ_g denotes the gas density.

Injecting droplets in DPM, the Species model is needed, and the Species transport model was used for the SARS CoV-2 droplets. The species transport equation for i[th] species [40]

$$\frac{\partial}{\partial t}(\rho Y_i) + \nabla.(\rho \vec{v} Y_i) = -\nabla.\vec{J_i} + R_i + S_i \tag{11}$$

where R_i and S_i is the net rate of production and rate of creation, respectively.

The mass diffusion is defined as[40];

$$\vec{J_i} = -(\rho D_{i,m} + \frac{\mu_t}{Sc_t})\nabla Y_i - D_{T,i}\frac{\nabla T}{T} \tag{12}$$

where Sc_t is the turbulent Schmidt number. Under the DPM model, the various sizes of Omicron droplets were injected at the surface of the mouth and nose to release all parts of the lung model based on various flow rates as mentioned earlier. The 'trap' boundary conditions were used for the airway wall, which means the particles were counted as trapped particles if they touch the wall. 41,210 droplets were injected at once, and the droplets' number convergence was calculated based on different sets of droplet injections. The density of the droplet is 1 g/cm^3. A stationary wall condition was used for the airway wall. Individual droplet trajectories and deposition positions were tracked by using a User Defined Function (UDF). A MATLAB code was used to post-process the deposition hot spot of the SARS CoV-2 droplets. The x, y, z coordinates of the deposited droplet were collected by UDF and MATLAB code was used to plot the deposition density curve.

Geometry Development

The extrathoracic airway model was generated from high-resolution CT-scan images. The digital image and communications in medicine (DICOM) images obtained from a healthy 30-year-old male were used to generate the realistic extrathoracic model. The de-identified CT-images were collected from the Taba-Parto Medical Imaging Center, Shiraz, Iran and proper ethical clearance was obtained from that authority.

Figure 1 shows the final 3-dimensional model and cross-sectional areas at different sections of the extrathoracic airways.

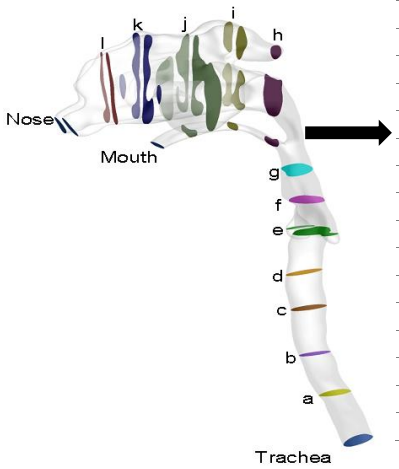

Cross-Section	Area (cm^2)
Trachea	1.37586
A	1.35742
B	0.868147
C	1.31058
D	1.19019
E	3.16498
F	2.21645
G	1.3783
H	4.49513
I	6.09508
J	16.4885
K	6.66692
L	2.69351
Mouth	0.4253
Nose	0.91382

Figure 1: Three-dimensional (3D) anatomical model and cross-sectional area at a randomly selected position of the extrathoracic airways.

Grid refinement and Validation

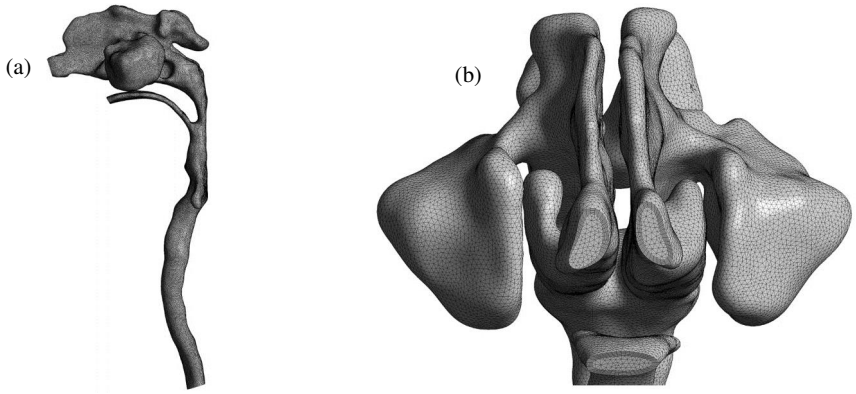

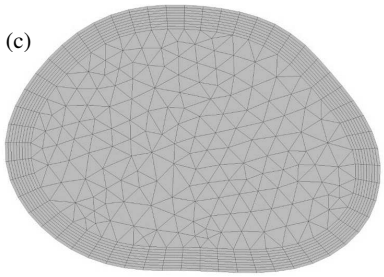

Figure 2: Unstructured computational mesh for the extrathoracic airway: (a) mesh for the whole domain, (b) Front view of the nasal cavities, and (c) inflation mesh at the outlet.

The computational element for the extrathoracic airway model is shown in Figure 2. The ANSYS meshing module was used for mesh construction. The unstructured tetrahedral elements were used for the highly complex and asymmetric extrathoracic airways. Inflation layers were used near the wall of the extrathoracic airways to capture the complex flow behaviour. Ten-layer inflations were used for the airway model. The grid independence was tested; the final model contained 4.3 million computational nodes.

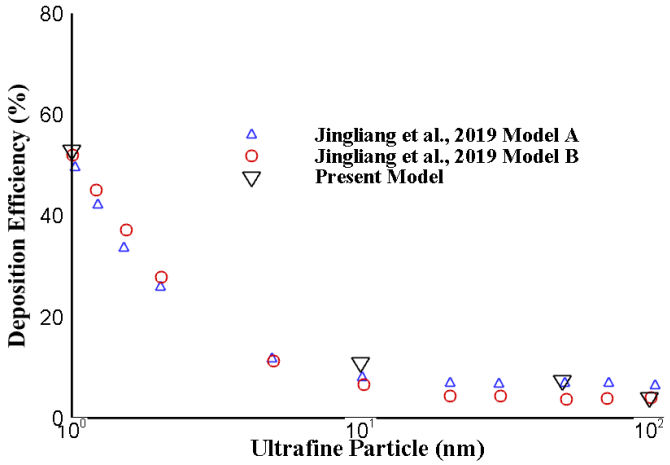

Figure 3: Ultrafine particles deposition efficiency (DE) comparison with reported literature at the extrathoracic airways [41]

The computational model was validated with the available benchmark experimental and numerical measurements. Figure 3 shows the ultrafine particle DE with the numerical data of Dong, et al.[41] . A range

of ultrafine-sized particle DE was calculated at 18 L/min flow rate. The ultrafine particle DE in the extraroracic airways shows a trend similar to the published data.

Fig. 4 shows the overall DE comparison in the extrathoracic airways with the available experimental and numerical measurements [42-49]. The DE for a wide range of particle sizes was calculated for 15 L/min and 30 L/min inhalation rates. The DE of the present model fits nicely within the range of the benchmark experimental and numerical data, which indicates the satisfactory accuracy of the present model.

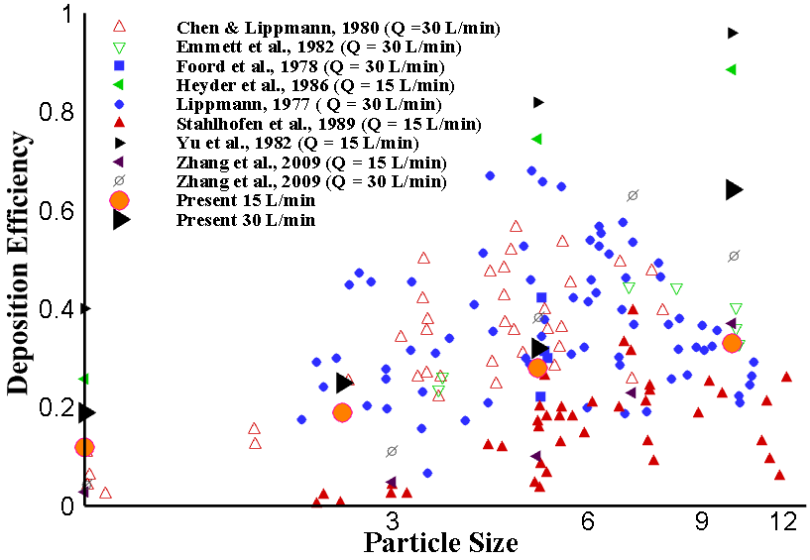

Figure 4. Deposition Efficiency (DE) comparison of micron size particles at the extrathoracic airways with available literature[43-50].

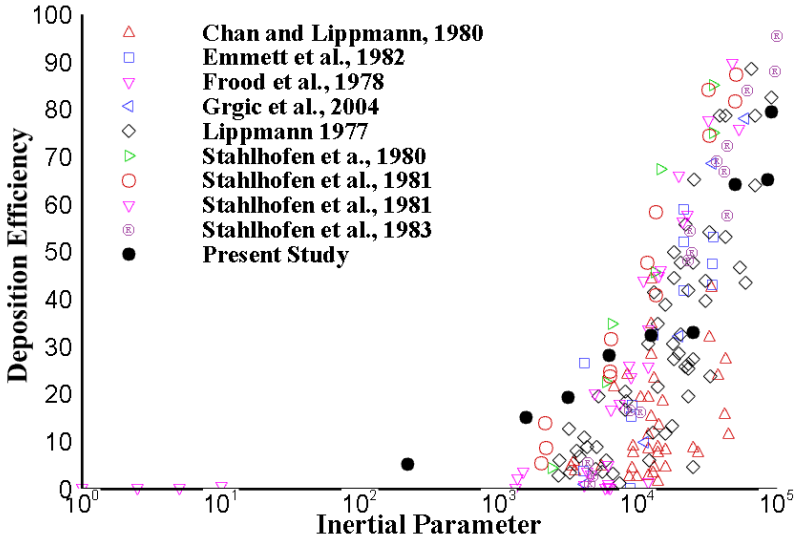

Figure 5. DE comparison of the inertial values at the extrathoracic airways with available literature[43, 45, 46, 48, 51-54].

Figure 5 presents the DE comparison as a function of the inertial parameter ($\rho d_p^2 Q$). The overall DE is compared with the benchmark experimental and computational models. The inertial parameter value was calculated for the low-flow rates of both smaller and larger diameter particles. The DE of the present model matches the available data, indicating the validity of the present numerical model.

Results and Discussions

The hydrodynamic characteristics of the flow and of SARS CoV-2 Omicron droplet deposition hotspots were analyzed and discussed in this Section. Several planes and lines were considered for data analysis and post-processing on different transverse cross-sections along the airflow path in the airways model. These planes and lines are demonstrated in Figure 6b, plane 1 is inside the nasal cavity, while plane 2 is located before the larynx in the airways. Plane 3 is placed at the main trachea some distance after the larynx, and plane 4 is considered to be on the main trachea before the first bifurcation.

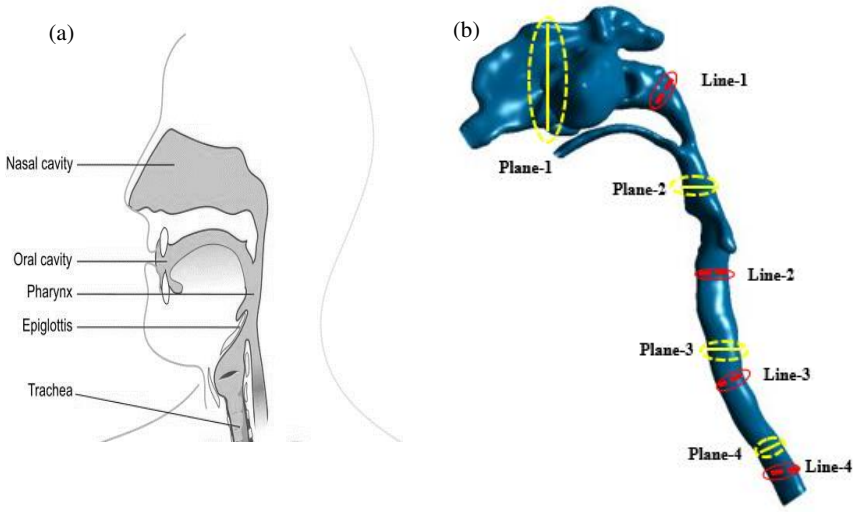

Figure 6. (a) Anterior view of the realistic extrathoracic airways, and (b) Randomly selected locations for the velocity profiles and contours.

Figure 7 depicts the velocity magnitude contours for different flow rates of 7.5, 15 and 30 L/min on the planes introduced in Figure 6b. Figure 7 shows the uniform momentum distribution in planes 3 and 4 in comparison with planes 1 and 2. However, the momentum distribution is more asymmetric on planes 1 and 2 due to the morphological complexity of airway geometry at the locations of planes 1 and 2. The airflow has a very tiny passage inside the nasal cavity, and the airway walls strongly influence the air velocity. The velocity is higher at the core of the cross-section on plane 1, and this region develops by increasing the flow rate as observed in Figures 7b, c for plane 1. A similar trend is observed on plane 2 where the flow is highly affected by the presence of the larynx downstream. Planes 3 and 4, however, are located in regions with less geometrical complexity, which is reflected in the velocity magnitude contours being more uniform than planes 1 and 2. Increasing the flow rate increases velocity magnitude on all planes and makes the momentum distribution more uniform on different planes, particularly on planes 3 and 4.

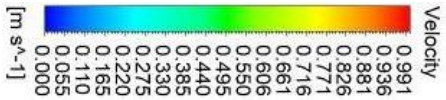

(a) (b) (c)

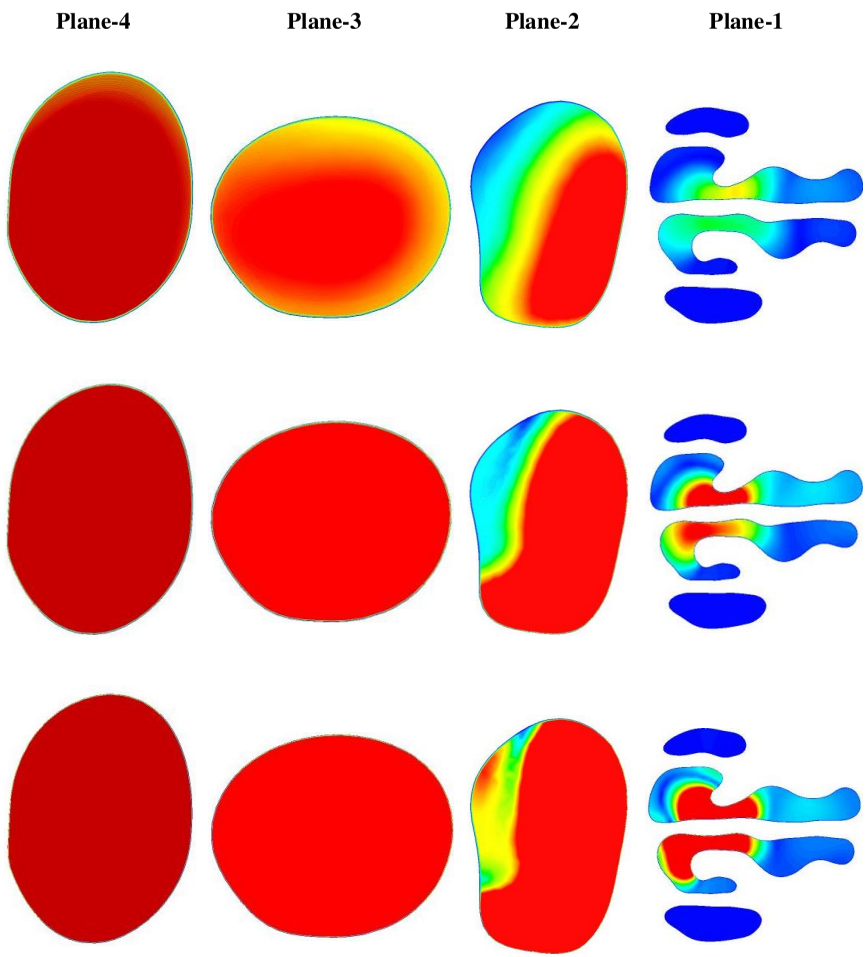

Figure 7. Velocity contours at different flow rates: (a) Q=7.5 L/min, (b) Q=15 L/min, and (c) Q=30 L/min (Figure 6 illustrates the plane).

The velocity profiles depicted in Figure 8 also support this fact. From this figure, the X-Position refers to the distance of the wall of the airways from one side to another side (refer to the location of each line), which was measured by the coordinate origin of the model. The velocity profiles for lines 1 and 2 are strongly distorted, intensifying the distortion with an increasing flow rate. However, the velocity profiles on lines 3 and 4 are moderately curved with more predictable behaviour. Among the velocity profiles depicted in Figure 8, the velocity profile of line 2 is the only profile with several extrema due to the larynx's presence, which has a smaller cross-section area. This results in airflow acceleration and generation of the laryngeal jet, which deviates the velocity profiles and creates an extremum at the middle of the line. Increasing flow rate impacts the velocity profile shape and the extrema generated.

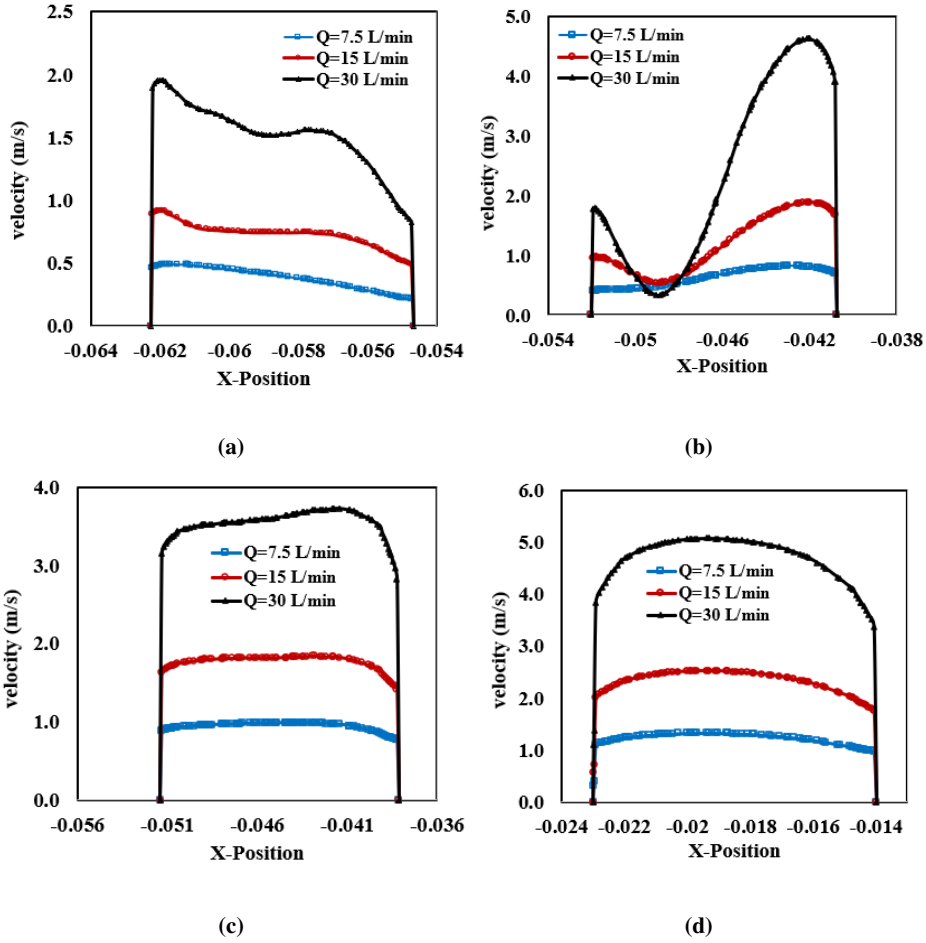

Figure 8. Velocity profiles at different flow rates, (a) Line-1, (b) Line -2, (c) Line-3, and (d) Line-4 (Figure 6 illustrates the lines).

The wall shear stress contours throughout the model are presented in Figure 9 at three flow rates of 7.5, 15 and 30 L/min. The shear stress depends on the velocity gradient on the wall, which is the direction perpendicular to the wall of the airways. Therefore, a higher flow rate is associated with a higher velocity gradient at the wall, resulting in higher wall shear. As observed in Figure 9, the wall shear increases with increasing the flow rate, which is why the shear is highest at a flow rate of 30 L/min in most parts of the model, such as the mouth-throat, larynx and the main trachea. Despite the effect of flow rate on wall shear, the local geometrical complexities also affect the wall shear in the model. Some regions are highly affected by wall shear such as the pharynx and the region after the larynx which is influenced by the laryngeal jet. This phenomenon is particularly more distinguished at a flow rate of 30 L/min.

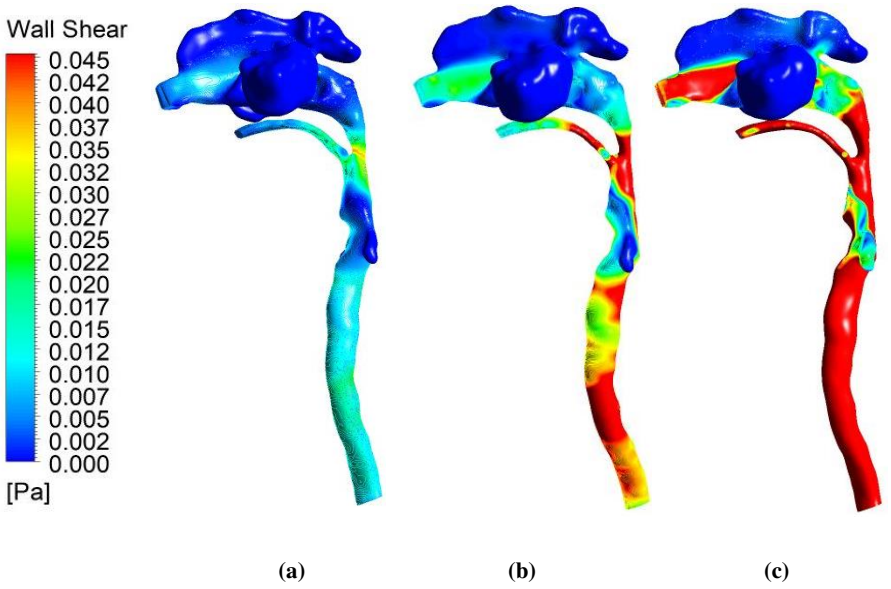

Figure 9. Wall shear for the different flow rates; (a) Q=7.5 L/min, (b) Q=15 L/min, and (c) Q=30 L/min

Despite the contours which present more qualitative data, Table 1 presents quantitative data of the maximum wall shear on planes 1-4. Table 1 also confirms the aforementioned analysis, as it can be seen that the maximum wall shear is the highest on plane 2 at all flow rates. This is due to the fact that plane 2

is located right after the larynx and is highly affected by the laryngeal jet. After plane 2, planes 4, 3 and 1 have the highest amounts of wall shear, showing that geometrical complexities influence the wall shear.

Table 1. Maximum wall shear for the different flow rates (the plane indicated in Figure 6).

	Q=7.5 L/min	Q=15 L/min	Q=30 L/min
Plane-1	0.0068	0.0198	0.0723
Plane-2	0.0248	0.0754	0.2599
Plane-3	0.0115	0.0351	0.1178
Plane-4	0.0141	0.0423	0.1472

Figure 10 demonstrates the average static pressure on various planes introduced in Figure 6 for different flow rates. The flow of air inside the airways is accompanied by loss of energy and hence pressure drop. Particularly, the complex shape of the air paths inside the model augments the energy loss and pressure drop. As shown in Figure10, the average static pressure reduces progressively for all flow rates as air moves deeper inside the airways. The highest pressure occurs on plane 1, which is located at the nasal cavity, and the lowest pressure is observed on plane 4, which is at the end of the main trachea right before the first generation. Another important point to note in Figure 10 is the significant effect of increasing the flow rate on the pressure, as the highest pressure is seen on plane 1 for the flow rate of 30 L/min. Higher pressure drop along the air path inside the airways is also a result of higher flow rate as demonstrated in Figure 10, pressure for the flow rate of 30 L/min falls drastically on different planes toward the deeper airways.

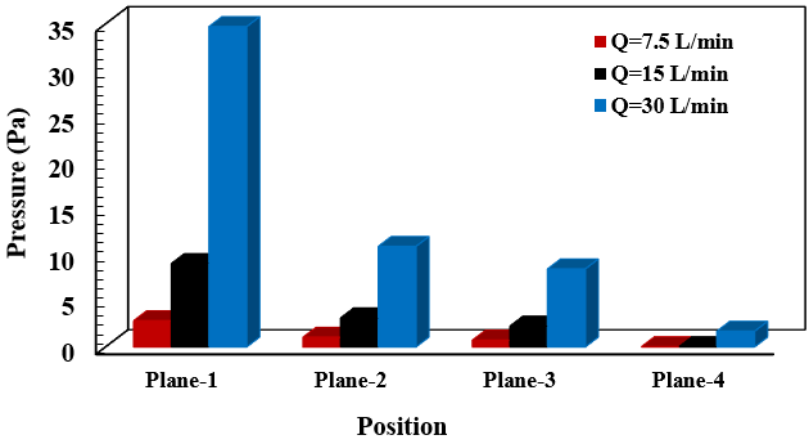

Figure 10. Pressure drop at three different flow rates in a different plane; the plane numbers are shown in Figure 6.

Turbulent intensity is a measurement of the turbulence level of the flow and is regarded as the root mean square of the fluctuations of the turbulent flow velocity normalised by the mean flow velocity. Therefore, it is a proper quantity for manifesting the turbulence level in a flow. The turbulent intensity contours are depicted in Figure 11 for different flow rates. The turbulent intensity rises at higher flow rates and that turbulent level is more intense at the pharynx, larynx, and main trachea. Table 2 presents quantitative data on the maximum turbulence intensity that occurs on different cross-sections of the airways passage. The maximum turbulence intensity on plane 2 is greater in all of the flow rates. Plane 2 is the pharynx region where the two air passages from the mouth and nasal cavity join together. It is indicated in Table 2 and the contours that the turbulent fluctuations of the flow are higher in this region in comparison with other parts of the airways. The larynx and the trachea are the regions where turbulence intensification is more remarkable.

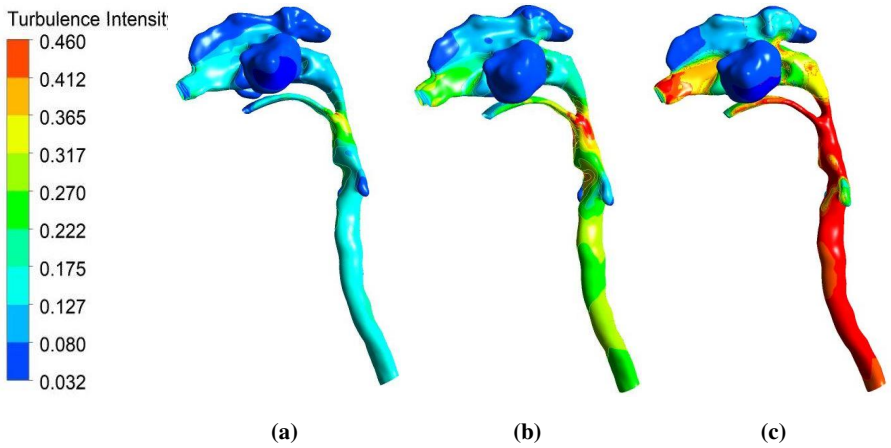

Figure 11. Turbulence intensity for the different flow rates; (a) Q=7.5 L/min, (b) Q=15 L/min, and (c) Q=30 L/min

Table 2. Maximum Turbulence intensity for the different flow rates (the plane indicated in Figure 6).

	Q=7.5 L/min	Q=15 L/min	Q=30 L/min
Plane-1	0.1604	0.2959	0.5095
Plane-2	0.3308	0.5892	1.1419
Plane-3	0.1783	0.3203	0.6374

Plane-4	0.1830	0.3028	0.5470

In order to better understand the flow field dynamics, flow streamlines are shown to be an efficient tool that can better present how morphological characteristics may affect the flow field. The geometry of respiratory airways is highly asymmetric with plenty of alternations in the airflow passage, which results in an intense disorder in the movement of the air stream. Figure 12 demonstrates the air flow streamlines in different regions of the respiratory airways at different flow rates, which presents a better view of streamlines in the nasal cavity and larynx due to their most influential role in the airflow path. These two regions have the most impression on the flow path which is due to the presence of turbinate and maxillary sinuses in the nasal cavity and the sudden reduction of flow cross-section in the larynx. At lower flow rates, the flow streamlines are smooth and more straightforward than at higher flow rates, and the flow direction does not frequently change inside the airways except that there is a slight distortion of streamlines in the nasal cavity and the larynx. However, with increasing flow rate, several vortices are generated inside the nasal cavity and the larynx (Figure 12b), which makes the flow circulate further in these regions. Increasing flow rate generates larger vortices inside the regions and makes the flow bend more and rapidly change direction. The highest velocity occurs in the pharynx, and the lowest velocity occurs for the air passing through the nasal cavity and maxillary sinuses, as shown in Figure 12. The most intricate streamlines are observed in Figure 12c, which occurs for the highest flow rate in this study.

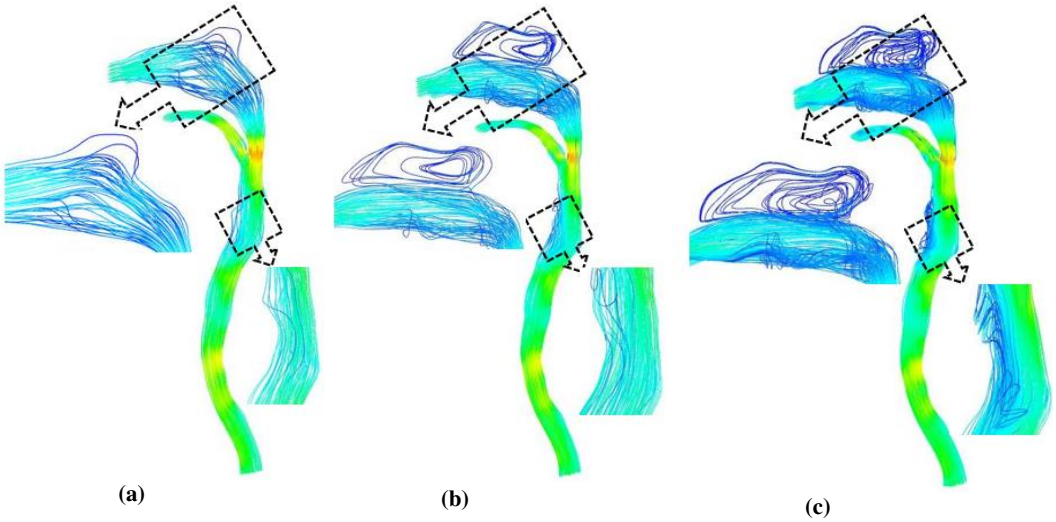

Figure 12. Velocity streamline for the different flow rates; (a) Q=7.5 L/min, (b) Q=15 L/min, and (c) Q=30 L/min

The goal of this study is an improved understanding of the transmission of SARS CoV-2 Omicron droplets under different physical activities in the extrathoracic airways. The deposition of SARS CoV-2 Omicron droplets of different sizes at different flow rates are depicted in Figure 13. For better presentation of the deposition patterns, the nasal cavity, which has more complex geometry, is focused on for a better view. In Figure 13, most SARS CoV-2 omicron droplets get trapped in the nasal and oral cavity, and fewer droplets can find their path to the lower airways, particularly for viral droplets of larger diameters. However, the number of viral droplets that deposit in the nasal cavity varies with droplet size and flow rate. At lower flow rate (Figure 13a), droplets of different sizes are deposited on the wall of the nasal cavity while the majority of deposited droplets have larger diameters in comparison to other droplets. However, by increasing the flow rate from 7.5 L/min to 15 L/min, obviously, a filtration effect takes place, and the SARS CoV-2 omicron droplets of larger diameters get trapped in the nasal and oral cavity, and fewer viral droplets of a diameter larger than 2.5 microns can pass through the intricate air passages towards the deeper airways. This phenomenon is more significant for the flow rate of 30 L/min, where most of the viral droplets of larger than 2.5 microns are deposited on the nasal cavity and oral cavity walls. It is also observed that the oral cavity is one of the most particular regions in terms of viral droplet deposition as it could be seen that the majority of 10-micron droplets in Figure 13c are deposited in the oral cavity. The foregoing results confirm that the most dominant deposition mechanism in the nasal and oral cavity is the impaction mechanism. Due to the complex geometry of airway passage at the nasal and oral cavity and frequent changes of curvature in the flow path, the viral droplets may not properly change their direction to avoid wall impaction and hence deposit on the wall. This incident is more intense for larger SARS CoV-2 omicron droplets with higher inertia, which cannot properly follow the flow streamlines, and are more prone to deposit at the initial stages of the respiratory airways. This finding is apparently illustrated in Figure 13c. Another important finding from Figure 13 is during passing the oral and nasal cavity and reaching the trachea, the particles tend to deposit mostly on the front wall of the trachea. This can be because of the gravity force which is acting upon theses viral droplets. This deposition mechanism is called gravitational sedimentation.

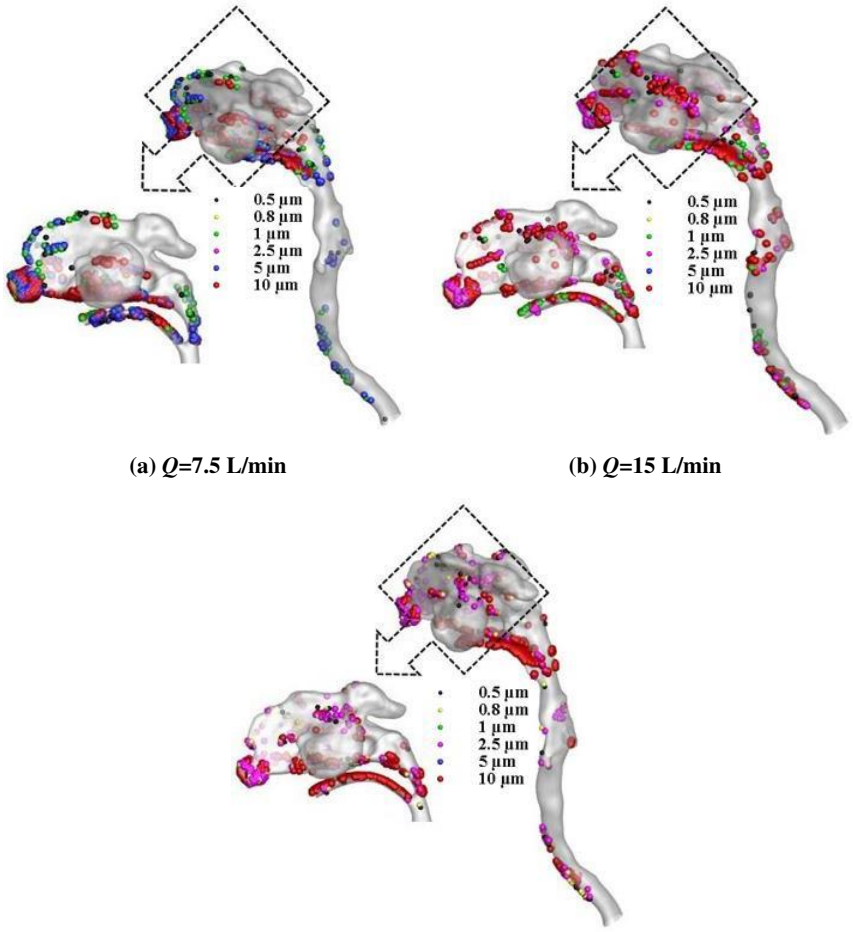

(a) Q=7.5 L/min **(b) Q=15 L/min**

(c) Q=30 L/min

Figure 13. Distribution of SARS CoV-2 Omicron droplet deposition in the extrathoracic airway model at a different flow rate; (a) Q=7.5 L/min, (b) Q=15 L/min, and (c) Q=30 L/min

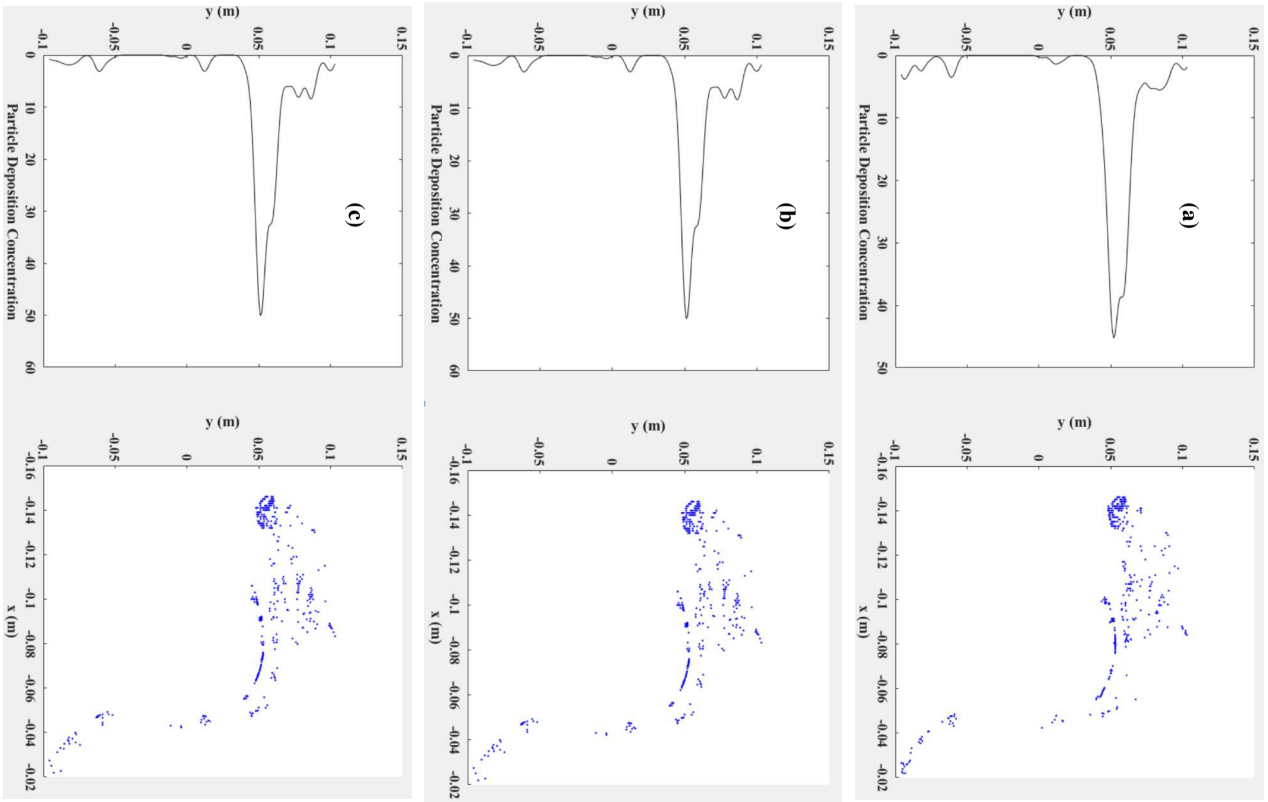

Figure 14. SARS CoV-2 Droplet deposition concentration at 30 L/min flow rate, (a) 500-nm (b) 800-nm, and (c) 2.5-µm.

Figure 14 depicts the deposition hotspots for three distinct virus droplet diameters: 500 nm, 800 nm and 2.5 µm with the flow rate of 30 L/min, the highest flow rate simulated in this study. This figure provides a better understanding of the deposition hotspots along the y-direction in the model. It gives a good insight into the deposition hotspots for each size of virus droplets separately. The deposition mainly occurs in the range of y = 0.03 m to y = 0.1 m which falls within the nasal cavity and oral cavity. The maximum deposition concentration at about y = 0.06 m is for the 800 nm and 2.5 µm virus droplets which affirms the previously mentioned results about the deposition mechanisms.

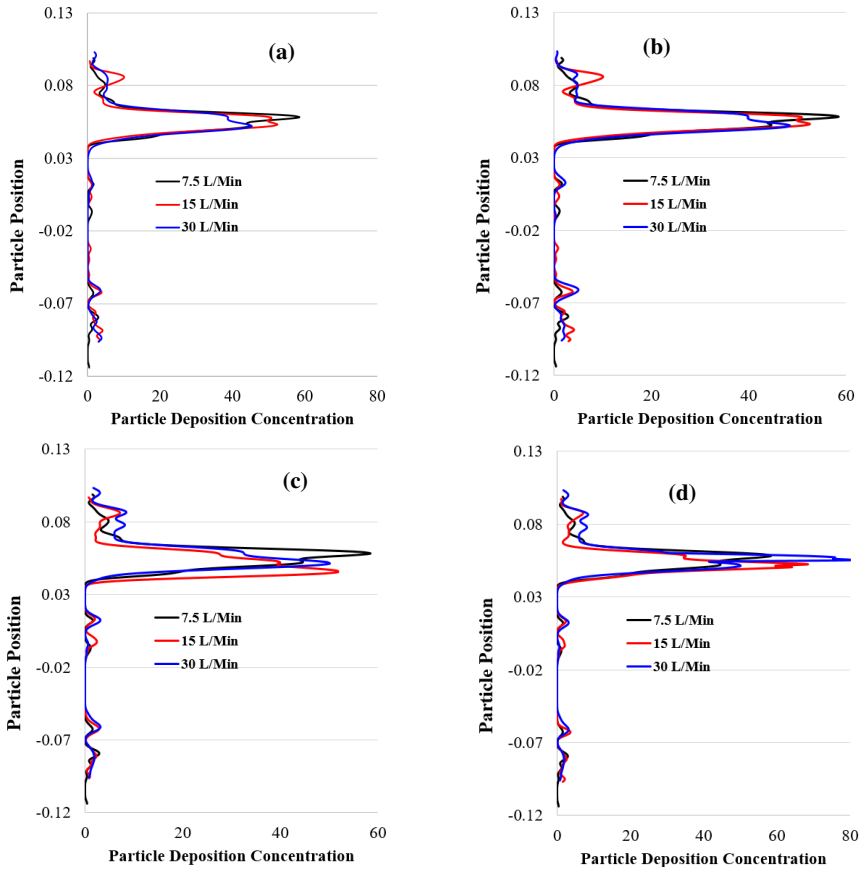

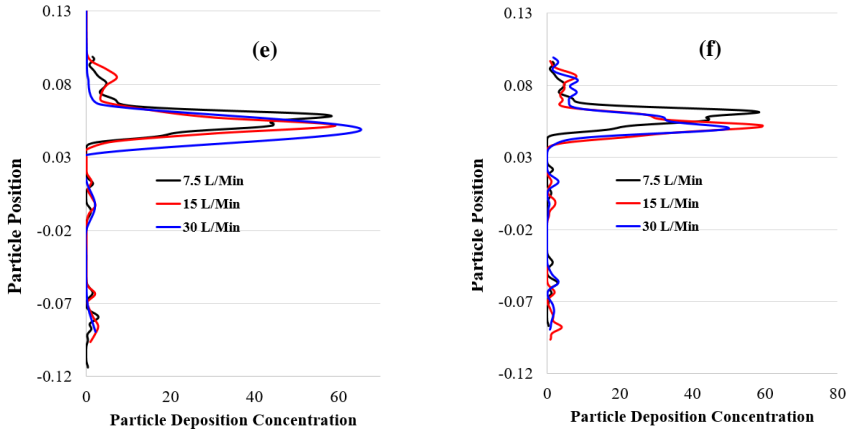

Figure 15. SARS CoV-2 droplet deposition concentration from inlets to the outlet of an extrathoracic model at various flow rates, (a) 500 nm, (b) 800 nm, (c) 1 µm, (d) 2.5 µm, (e) 5 µm, and (f) 10 µm.

Figure 16 depicts the toxicity of the SARS CoV-2 droplets for different virus droplet sizes of 500 nm and 10 µm for different flow rates of 7.5 L/min, 15 L/min and 30 L/min. The droplet toxicity is associated with the velocity of virus droplets upon their impact on the wall of airways. These results can provide a deeper insight on how the deposition of SARS CoV-2 droplets in different regions of airways may cause health issues. Figures 16 a, b and c, which are the toxicity results for the 500 nm virus droplets at different flow rates, indicate that most viral droplets with higher velocity deposition occur at the nasal cavity entrance, called the vestibules. This could be due to the highly deformed morphology of the airway at the entrance of the nasal cavity, which causes a sudden change of direction in the air passage and forces the droplets to impact the wall at a higher velocity. The deposition at other regions for 500 nm SARS CoV-2 droplet occurs at lower velocity. For 10 µm SARS CoV-2 droplets (Figures16, d, e, f), the high-velocity impact of viral droplets is observed to occur at the entrance of the nasal vestibules; however other viral droplets with lower velocity wall impact are occurred at the oropharynx. It is shown that the flow rate considerably affects the deposition hotspot for 10 µm virus droplets as the concentration of droplets becomes more remarkable in the oropharynx region.

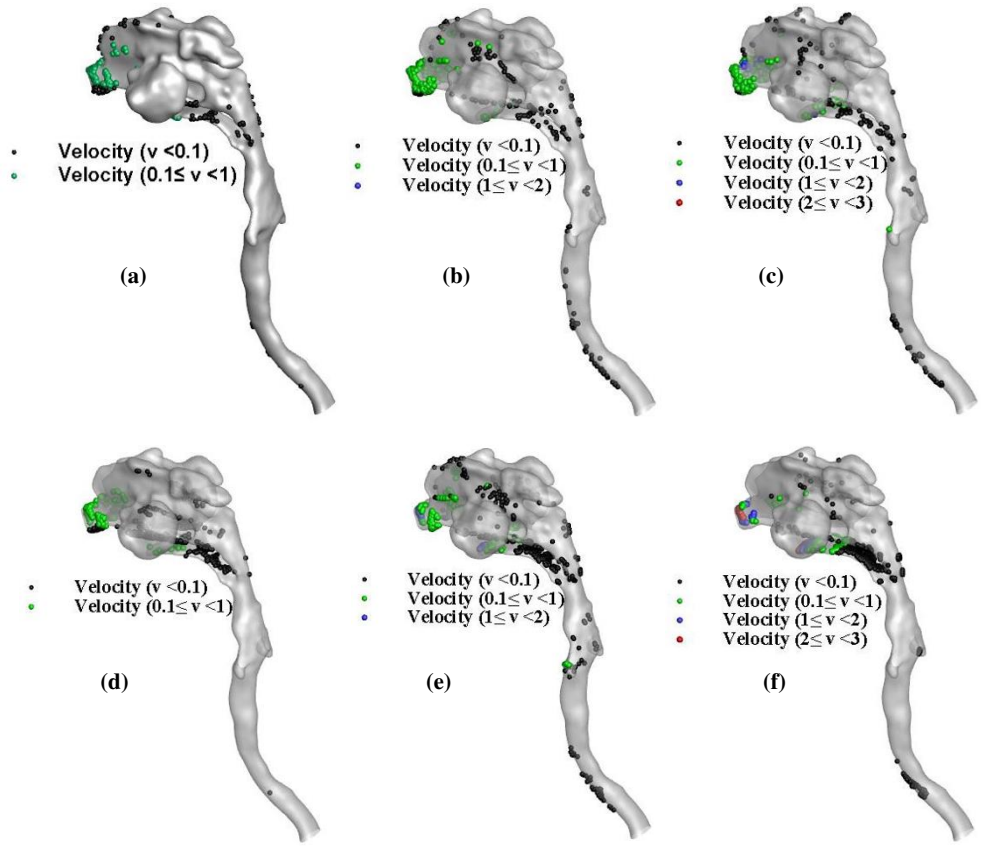

Figure 16. Toxicity of SARS CoV-2 Omicron droplet in the extrathoracic airways at different flow rates; (a) d_p=500 nm, Q=7.5 L/min, (b) d_p=500 nm, Q=15 L/min, (c) d_p=500 nm, Q=30 L/min, (d) d_p=10 μm, Q=7.5 L/min, (e) d_p=10 μm, Q=15 L/min, and (f) d_p=10 μm, Q=30 L/min.

Table 3 presents the total deposition data for the 500 nm and 10 μm SARS CoV-2 droplets at different flow rates for mouth inhalation and nose inhalation separately. The total deposition efficiency of 10-micron droplets is observed to be higher than the 500 nm droplets at all flow rates. Another important point is that the nose inhalation deposition efficiency is higher for both 500-nm and 10 μm SARS CoV-2 droplets at flow rates of 7.5 L/min and 15 L/min except for flow rate of 30 L/min. At the flow rate of 30 L/min, the nose inhalation droplet deposition exceeds the mouth inhalation deposition only for the 500-nm droplets, while for 10-micron droplets, it is the opposite. The deposition for mouth inhalation is higher than the nose

inhalation deposition. This could be due to the curved path that droplets need to take to pass the oral cavity. The larger diameter and higher gravity force on them make them incapable of following the flow streamlines properly and depositing on the oral cavity surface. This phenomenon is better demonstrated in Figure 17b, which depicts the deposition hotspot for 10-micron virus droplets at the flow rate of 30 L/min. As seen in this figure, the deposited droplets are mainly concentrated on the bottom of the oral cavity.

Table 3. Deposition efficiency analysis for the mouth and nose regions at different flow rates

	Deposition efficiency (%)					
	Q=7.5 L/min		*Q*=15 L/min		*Q*=30 L/min	
	500 nm	10 μm	500 nm	10 μm	500 nm	10 μm
Inhalation (Nose)	9.785	16.742	9.368	12.627	8.631	10.456
Inhalation (Mouth)	2.389	3.675	2.221	8.593	2.289	17.889

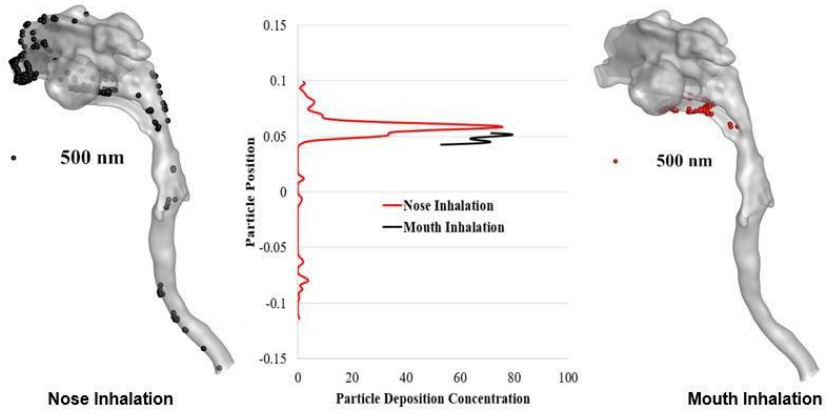

Figure 17. 500 nm SARS CoV-2 droplet deposition during mouth and nose inhalation and corresponding deposition hot spot at extrathoracic airways at 7.5 L/min flow rate.

Figures 17 and 18 demonstrate the deposition hotspots of the 500 nm and 10 μm SARS CoV-2 droplets at a flow rate of 7.5 L/min for the mouth and nose inhalation separately. Obviously, the depositions of 10 μm droplets in both the mouth and nose inhalations are higher than 500 nm droplets. Figures 17-18 also reveal that the viral droplets inside the nasal cavity disperse more evenly in the nose inhalation than in the mouth inhalation. This is because most of the deposited viral droplets are concentrated in one region. One important finding is that penetration of the viral droplets to the lower airways for nose inhalation is higher than the mouth inhalation, meaning nose inhalation could cause a higher vulnerability for viral infection

than mouth inhalation. In mouth inhalation, the 500 nm viral droplets can better penetrate the deeper airways than the nose inhalation case at the 7.5 L/min flow rate. This could be due to the weakening of the Brownian diffusion effect at a higher flow rate, resulting in the lower deposition. This phenomenon is supported by the data presented in Table 3. The deposition of 500 nm viral droplets at 7.5 L/min in mouth inhalation is 2.389% which is higher than the 30 L/min 500 nm deposition, being 2.289%.

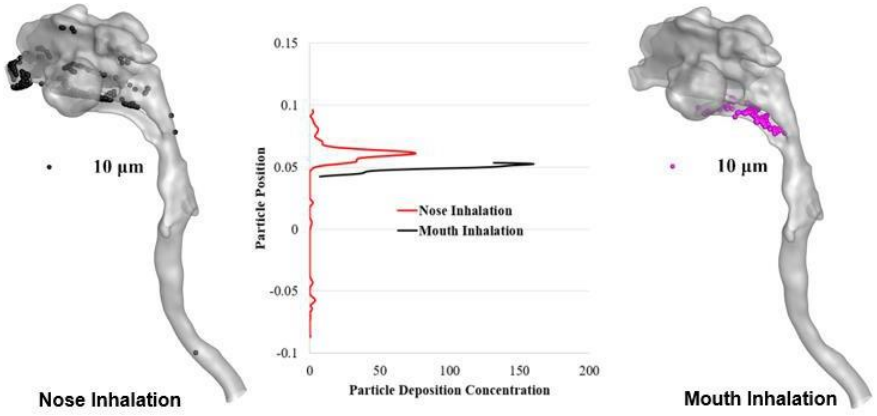

Figure 18. 10 µm SARS CoV-2 Omicron droplet deposition during mouth and nose inhalation and corresponding deposition hot spot at extrathoracic airway at 7.5 L/min flow rate.

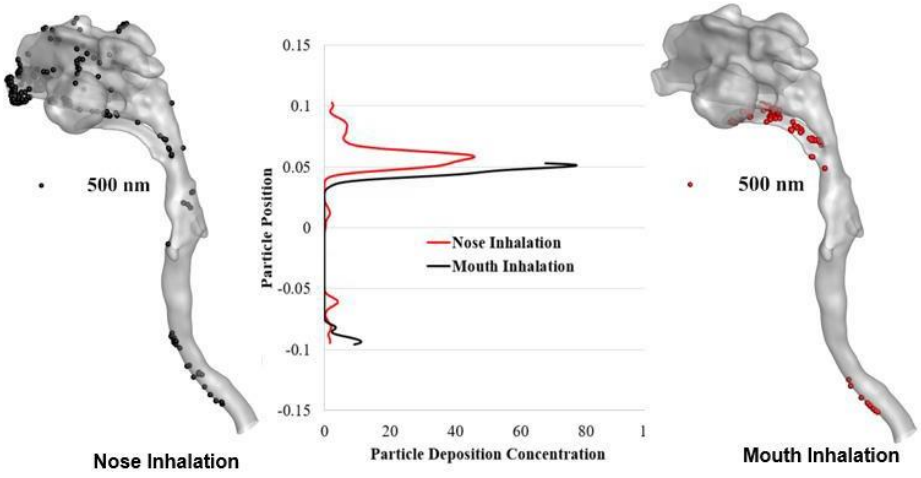

Figure 19. 500 nm SARS CoV-2 Omicron droplet deposition during the mouth and nose inhalation and corresponding deposition hot spot at extrathoracic airways at 30 L/min flow rate.

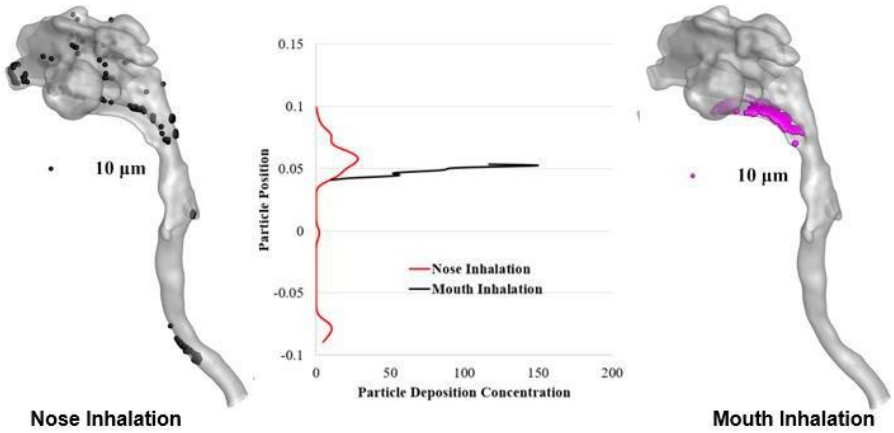

Figure 20. 10 µm SARS CoV-2 Omicron droplet deposition during the mouth and nose inhalation and corresponding deposition hot spot at extrathoracic airway at 30 L/min flow rate.

Figure 19 shows the deposition hot spot of the 500 nm size SARS CoV-2 droplets at a high flow rate. The deposition concentration plot shows that the overall SARS CoV-2 droplet deposition density during mouth inhalation at the pharynx region is significantly higher than during the nose inhalation method. No viral droplets are deposited at the epiglottal region during the mouth inhalation. However, the SARS CoV-2 droplet is deposited at the tracheal section of the airways. Therefore, SARS CoV-2 droplets are deposited throughout the nasal cavities, pharyngeal, epiglottal and tracheal regions for nose inhalation.

For larger diameter SARS CoV-2 droplets, at a high flow rate (30 L/min), the mouth inhalation shows a high virus concentration in the pharynx region, as shown in Fig. 20. The deposition concentration of the virus in the pharyngeal area is significantly higher than in nose inhalation. However, SARS CoV-2 droplets are deposited in the tracheal area along with the nasal cavities for nose inhalation. The comprehensive analysis of the SARS CoV-2 droplet deposition at different sections of the extrathoracic airways during mouth and nose inhalations would improve the knowledge of the viral deposition hot spot. These specific findings could potentially improve the health risk assessment of the covid patients and the development of the airway zone and patient-specific targeted drug delivery methods.

Conclusions

The SARS CoV-2 Omicron droplet deposition to the realistic extrathoracic numerical airways model is discussed. The comprehensive investigations are performed for various physical activities. The key findings of the numerical study are listed below;

- A maximum of 33.01% of pressure drop is observed in the 30-L/min inlet condition. The overall pressure drop on different planes toward the deeper airways drops with flow rate;
- The maximum turbulence intensity is observed at the pharyngeal area. The turbulence intensity at 30- L/min flow rate is 3.45 times higher than at the 7.5-L/min flow rate;
- For the 500nm-SARS CoV-2 Omicron droplets, the deposition rates at the nose and mouth are 9.78 % and 2.39%, respectively. The overall DE for the nose inhalation is significantly higher than for the mouth inhalation;
- At a SARS CoV-2 Omicron droplet size of d_p=10 μm, the deposition rate at nasal cavities decreased with the increase flow rate;
- At a resting condition (7.5 L/min), the smaller diameter SARS CoV-2 Omicron droplets are mainly deposited at the nasal cavities and mouth-throat regions. At a high-flow rate (30 L/min), the larger-diameter droplets are mostly deposited in the extrathoracic airways.
- The SARS CoV-2 Omicron droplet toxicity at the nasal cavities is higher than in the mouth-throat region. In the tracheal region, the SARS CoV-2 Omicron droplet toxicity is found to be lower than in the upper region, which confirms that the SARS CoV-2 Omicron is hazardous for the upper extrathoracic airways.
- The deposition density curve for the SARS CoV-2 Omicron droplets demonstrates the high concentration of the virus at the mouth-throat region during mouth inhalation. This comprehensive analysis is highly critical for the health risk assessment of the covid patients.

This study comprehensively analyzed the SARS CoV-2 Omicron droplet transport and deposition behaviour in the extrathoracic airways. Findings of this study with more patient-specific cases would improve the Omicron droplet transport in the extrathoracic airways. The future study may experimentally analyze the Omicron droplet transport in patient-specific airways.

Conflicts of Interest: The authors declare no conflicts of interest.

Ethical Clearance: All procedures performed in studies involving human participants were in accordance with the ethical standards of the institutional and/or national research committee and with the 1964 Helsinki declaration and its later amendments or comparable ethical standards.

Acknowledgements: The authors acknowledge Distinguished Professor **Lidia Morawska** and her International Laboratory for Air Quality and Health, Queensland University of Technology, 4000,

Brisbane, Australia, for comments on this manuscript. The high-performance computing facility at UTS is also highly acknowledged.

Data Availability Statement: Data will be available upon reasonable request

References

1. Z. Yousaf, M. A. Khan, M. S. Asghar, M. Zaman, M. Ahmed, andM. J. Tahir, "COVID-19 Omicron variant-Time for airborne precautions," Annals of Medicine and Surgery 103919 (2022).

2. M. S. Islam, P. Larpruenrudee, A. R. Paul, G. Paul, T. Gemci, Y. Gu, andS. C. Saha, "SARS CoV-2 aerosol: How far it can travel to the lower airways?," Physics of Fluids **33**, 061903 (2021).

3. H. M. Beni, H. Mortazavi, andM. S. Islam, "Biomedical and biophysical limits to mathematical modeling of pulmonary system mechanics: a scoping review on aerosol and drug delivery," Biomechanics and Modeling in Mechanobiology 1 (2021).

4. L. Morawska, andJ. Cao, "Airborne transmission of SARS-CoV-2: The world should face the reality," Environment international **139**, 105730 (2020).

5. R. Dhand, andJ. Li, "Coughs and sneezes: their role in transmission of respiratory viral infections, including SARS-CoV-2," American journal of respiratory and critical care medicine **202**, 651 (2020).

6. A. J. Keeley, C. M. Evans, andT. I. De Silva, "Asymptomatic SARS-CoV-2 infection: the tip or the iceberg?," Thorax **75**, 621 (2020).

7. S. L. Miller, W. W. Nazaroff, J. L. Jimenez, A. Boerstra, G. Buonanno, S. J. Dancer, J. Kurnitski, L. C. Marr, L. Morawska, andC. Noakes, "Transmission of SARS-CoV-2 by inhalation of respiratory aerosol in the Skagit Valley Chorale superspreading event," Indoor air **31**, 314 (2021).

8. C. Karagiannidis, C. Mostert, C. Hentschker, T. Voshaar, J. Malzahn, G. Schillinger, J. Klauber, U. Janssens, G. Marx, andS. Weber-Carstens, "Case characteristics, resource use, and outcomes of 10 021 patients with COVID-19 admitted to 920 German hospitals: an observational study," The Lancet Respiratory Medicine **8**, 853 (2020).

9. A. Hartmann, J. Lange, H. Rotheudt, andM. Kriegel, "Emission rate and particle size of bioaerosols during breathing, speaking and coughing," (2020).

10. J. K. Gupta, C. H. Lin, andQ. Chen, "Flow dynamics and characterization of a cough," Indoor air **19**, 517 (2009).

11. G. Johnson, L. Morawska, Z. Ristovski, M. Hargreaves, K. Mengersen, C. H. Chao, M. Wan, Y. Li, X. Xie, andD. Katoshevski, "Modality of human expired aerosol size distributions," Journal of Aerosol Science **42**, 839 (2011).

12. H. Mortazavy Beni, H. Mortazavi, E. Tashvighi, andM. S. Islam, "Investigation of the Upper Respiratory Tract of a Male Smoker with Laryngeal Cancer by Inhaling Air Associated with Various Physical Activity Levels," Atmosphere **13**, 717 (2022).

13. M. Rahimi-Gorji, C. Debbaut, G. Ghorbaniasl, S. Cosyns, W. Willaert, andW. Ceelen, "Optimization of intraperitoneal aerosolized drug delivery using computational fluid dynamics (CFD) modeling," Scientific Reports **12**, 1 (2022).

14. J. Heyder, J. Gebhart, G. Heigwer, C. Roth, andW. Stahlhofen, "Experimental studies of the total deposition of aerosol particles in the human respiratory tract," Journal of Aerosol Science **4**, 191 (1973).

15. G. Ferron, S. Dua, E. Karg, W. Kreyling, T. Tuch, andJ. Heyder, "Estimation of the deposition of polydisperse hygroscopic aerosol particles in the respiratory tract," Journal of Aerosol Science **22**, S863 (1991).

16. Y.-S. Cheng, Y. Zhou, andB. T. Chen, "Particle deposition in a cast of human oral airways," Aerosol Science & Technology **31**, 286 (1999).

17. Y. Zhou, andY.-S. Cheng, "Particle deposition in a cast of human tracheobronchial airways," Aerosol Science and Technology **39**, 492 (2005).

18. K. A. Prather, C. C. Wang, andR. T. Schooley, "Reducing transmission of SARS-CoV-2," Science **368**, 1422 (2020).

19. S. Shao, D. Zhou, R. He, J. Li, S. Zou, K. Mallery, S. Kumar, S. Yang, andJ. Hong, "Risk assessment of airborne transmission of COVID-19 by asymptomatic individuals under different practical settings," Journal of aerosol science **151**, 105661 (2021).

20. L. Gradoń, D. Orlicki, andA. Podgorski, "Deposition and retention of ultrafine aerosol particles in the human respiratory system. Normal and pathological cases," International Journal of Occupational Safety and Ergonomics **6**, 189 (2000).

21. M. S. Islam, P. Larpruenrudee, S. C. Saha, O. Pourmehran, A. R. Paul, T. Gemci, R. Collins, G. Paul, andY. Gu, "How severe acute respiratory syndrome coronavirus-2 aerosol propagates through the age-specific upper airways," Physics of Fluids **33**, 081911 (2021).

22. M. Rahman, M. Zhao, M. S. Islam, K. Dong, andS. C. Saha, "Numerical study of nano and micro pollutant particle transport and deposition in realistic human lung airways," Powder Technology **402**, 117364 (2022).

23. L. Weaver, A. Das, S. Saffaran, N. Yehya, T. E. Scott, M. Chikhani, J. G. Laffey, J. G. Hardman, L. Camporota, andD. G. Bates, "High risk of patient self-inflicted lung injury in COVID-19 with frequently encountered spontaneous breathing patterns: a computational modelling study," Annals of intensive care **11**, 1 (2021).

24. M. M. Rahman, M. Zhao, M. S. Islam, K. Dong, andS. C. Saha, "Numerical study of nanoscale and microscale particle transport in realistic lung models with and without stenosis," International Journal of Multiphase Flow **145**, 103842 (2021).

25. V. K. Srivastav, A. R. Paul, andA. Jain, "Capturing the wall turbulence in CFD simulation of human respiratory tract," Mathematics and computers in simulation **160**, 23 (2019).

26. H. K. Versteeg, andW. Malalasekera, *An introduction to computational fluid dynamics: the finite volume method* (Pearson education, 2007).

27. M. Rahimi-Gorji, L. Van de Sande, C. Debbaut, G. Ghorbaniasl, H. Braet, S. Cosyns, K. Remaut, W. Willaert, andW. Ceelen, "Intraperitoneal aerosolized drug delivery: technology, recent developments, and future outlook," Advanced Drug Delivery Reviews **160**, 105 (2020).

28. V. Kumar, S. Saini, M. Sharma, andK. Nigam, "Pressure drop and heat transfer study in tube-in-tube helical heat exchanger," Chemical Engineering Science **61**, 4403 (2006).

29. M. Rahimi Gorji, C. Debbaut, W. Willaert, P. Segers, G. Ghorbaniasl, andW. Ceelen, *A numerical simulation of pressurized intraperitoneal aerosol chemotherapy (PIPAC): validation part* (2020).

30. M. R. Gorji, C. Debbaut, G. Ghorbaniasl, W. Willaert, S. Cosyns, andW. Ceelen, "Electrostatic precipitation pressurized intraperitoneal aerosol chemotherapy (ePIPAC): finding the optimal electrical potential," European Journal of Surgical Oncology **47**, e30 (2021).

31. P. Bradshaw, "Turbulent secondary flows," Annual review of fluid mechanics **19**, 53 (1987).

32. I. Larsson, E. Lindmark, T. S. Lundström, andG. Nathan, "Secondary flow in semi-circular ducts," Journal of fluids engineering **133**, (2011).

33. V. Stadnytskyi, P. Anfinrud, andA. Bax, "Breathing, speaking, coughing or sneezing: What drives transmission of SARS-CoV-2?," Journal of Internal Medicine **290**, 1010 (2021).

34. M. R. Gorji, S. Cosyns, C. Debbaut, G. Ghorbaniasl, W. Willaert, andW. Ceelen, "Analysis of the effect of liquid viscosity on the aerosol distribution during Pressurized Intraperitoneal Aerosol Chemotherapy (PIPAC) using computational modeling," European Journal of Surgical Oncology **48**, e159 (2022).

35. M. M. Rahman, M. Zhao, M. S. Islam, K. Dong, andS. C. Saha, "Nanoparticle transport and deposition in a heterogeneous human lung airway tree: An efficient one path model for CFD simulations," European Journal of Pharmaceutical Sciences **177**, 106279 (2022).

36. A. Haider, andO. Levenspiel, "Drag coefficient and terminal velocity of spherical and nonspherical particles," Powder technology **58**, 63 (1989).

37. K. Inthavong, K. Zhang, andJ. Tu, "Numerical modelling of nanoparticle deposition in the nasal cavity and the tracheobronchial airway," Computer Methods in Biomechanics and Biomedical Engineering **14**, 633 (2011).

38. A. Li, andG. Ahmadi, "Dispersion and deposition of spherical particles from point sources in a turbulent channel flow," Aerosol science and technology **16**, 209 (1992).

39. M. M. Rahman, M. Zhao, M. S. Islam, K. Dong, andS. C. Saha, "Aerosol Particle Transport and Deposition in Upper and Lower Airways of Infant, Child and Adult Human Lungs," Atmosphere **12**, 1402 (2021).

40. M. S. Islam, Y. Gu, A. Farkas, G. Paul, andS. C. Saha, "Helium–oxygen mixture model for particle transport in CT-based upper airways," International journal of environmental research and public health **17**, 3574 (2020).

41. J. Dong, J. Li, L. Tian, andJ. Tu, "Transport and deposition of ultrafine particles in the upper tracheobronchial tree: a comparative study between approximate and realistic respiratory tract models," Computer Methods in Biomechanics and Biomedical Engineering **24**, 1125 (2021).

42. M. El Hassan, H. Assoum, N. Bukharin, H. Al Otaibi, M. Mofijur, andA. Sakout, "A review on the transmission of COVID-19 based on cough/sneeze/breath flows," The European Physical Journal Plus **137**, 1 (2022).

43. T. L. CHAN, andM. LIPPMANN, "Experimental measurements and empirical modelling of the regional deposition of inhaled particles in humans," American Industrial Hygiene Association Journal **41**, 399 (1980).

44. W. Stahlhofen, G. Rudolf, andA. James, "Intercomparison of experimental regional aerosol deposition data," Journal of Aerosol Medicine **2**, 285 (1989).

45. P. Emmett, R. Aitken, andW. Hannan, "Measurements of the total and regional deposition of inhaled particles in the human respiratory tract," Journal of Aerosol Science **13**, 549 (1982).

46. N. Foord, A. Black, andM. Walsh, "Regional deposition of 2.5–7.5 μm diameter inhaled particles in healthy male non-smokers," Journal of Aerosol Science **9**, 343 (1978).

47. J. Heyder, J. Gebhart, G. Rudolf, C. F. Schiller, andW. Stahlhofen, "Deposition of particles in the human respiratory tract in the size range 0.005–15 μm," Journal of aerosol science **17**, 811 (1986).

48. M. Lippmann, "Pulmonary reactions to drugs," The Medical Clinics of North America **61**, 1353 (1977).

49. Z. Zhang, C. Kleinstreuer, andC. S. Kim, "Comparison of analytical and CFD models with regard to micron particle deposition in a human 16-generation tracheobronchial airway model," Journal of Aerosol Science **40**, 16 (2009).

50. C. Yu, andC. Diu, "A comparative study of aerosol deposition in different lung models," American Industrial Hygiene Association Journal **43**, 54 (1982).

51. W. Stahlhofen, J. Gebhart, andJ. Heyder, "Experimental determination of the regional deposition of aerosol particles in the human respiratory tract," American Industrial Hygiene Association Journal **41**, 385 (1980).

52. W. Stahlhofen, J. Gebhart, J. Heyder, andG. Scheuch, "New regional deposition data of the human respiratory tract," Journal of Aerosol Science **14**, 186 (1983).

53. B. Grgic, W. Finlay, andA. Heenan, "Regional aerosol deposition and flow measurements in an idealized mouth and throat," Journal of Aerosol Science **35**, 21 (2004).

54. W. Stahlhofen, J. Gebhart, andJ. Heyder, "Biological variability of regional deposition of aerosol particles in the human respiratory tract," American Industrial Hygiene Association Journal **42**, 348 (1981).